• Basic Research •

Angiogenesis-RNA modification in diabetic retinopathy: biomarkers and targets

Xue Wang[1], Dan-Ping Wu[2], Wei Du[1], Rui Li[1], Wei Lou[3], Ran-Ran Chen[2], Yu-Jie Liao[2], Qian Li[1], Xiao-Mei Li[2], Hong-Ping Cui[1], Jin-Ling Zhang[2]

[1]Department of Ophthalmology, Shanghai East Hospital, School of Medicine, Tongji University, Shanghai 200120, China

[2]Department of Ophthalmology, Shanghai Fifth People's Hospital, Fudan University, Shanghai 200240, China

[3]Department of Ophthalmology, Shanghai Sixth People's Hospital Affiliated to Shanghai Jiao Tong University School of Medicine, Shanghai 200233, China

Co-first Authors: Xue Wang and Dan-Ping Wu

Correspondence to: Hong-Ping Cui. No.150 Jimo Road, Pudong New District, Shanghai 200120, China. hpcui@vip.163.com; Jin-Ling Zhang. No.801 Heqing Road, Minhang District, Shanghai 200240, China. sahaleen@aliyun.com

Received: 2025-08-05 Accepted: 2026-07-01

Abstract

● **AIM:** To identify biomarkers and potential therapeutic targets related to angiogenesis and RNA modification in diabetic retinopathy (DR).

● **METHODS:** The Gene Expression Omnibus (GEO) datasets GSE12610, GSE87433, and GSE111465, which contain retinal samples from diabetic and normal mice, were analyzed to identify differentially expressed genes (DEGs). The DEGs were then intersected with angiogenesis- and RNA modification-related genes (A&RMRGs) obtained from GeneCards and other databases to identify differentially expressed A&RMRGs in DR. Hub genes were subsequently identified from the protein-protein interaction (PPI) network built on the enrichment results. Their diagnostic value was then estimated by receiver operating characteristic (ROC) analysis, and their expression levels were tested for associations with immune cell infiltration. Regulatory networks of hub genes were constructed using MicroRNA Target Prediction Database (miRDB), ChIPBase, and the Comparative Toxicogenomics Database (CTD). To validate the bioinformatic findings, hub gene transcript levels were quantified with reverse transcription quantitative polymerase chain reaction (RT-qPCR) in high-glucose-treated rat retinal microvascular endothelial cells (rRMECs).

● **RESULTS:** Forty-two A&RMRGs showed differential expression in the diabetic retina, with Gene Ontology (GO)/Kyoto Encyclopedia of Genes and Genomes (KEGG) enrichment implicating RNA modification and immune-inflammatory regulation, alongside Gene Set Enrichment Analysis (GSEA) evidence of activated RNA-silencing and fatty-acid-transport programs and suppressed neuronal and retinoid-cycle programs. Seven hub genes (*Wdr3*, *Crebbp*, *Sdad1*, *Stat3*, *Gnl2*, *Nhp2*, and *Hsp90aa1*) were selected, all of them were upregulated in DR. The DR retina showed higher levels of central memory $CD8^+$ T cells and lower levels of monocytes, Tregs, and $CD56^{bright}$ natural killer (NK) cells. Monocyte infiltration was inversely associated with *Stat3* expression (r=-0.604, P<0.001), and central memory $CD8^+$ T cell levels were positively associated with *Nhp2* expression (r=0.539, P=0.003). A total of 60 miRNAs, 43 transcription factors (TFs), and 47 drugs may regulate RNA modification of angiogenesis-associated genes in DR. *Gnl2* [area under the ROC curve (AUC)=0.914, 95% confidence interval (CI): 0.810–1.000) and *Stat3* (AUC=0.964, 95%CI: 0.892–1.000) showed high diagnostic value. Exposure of rRMECs to high glucose led to a marked rise in *Stat3* expression and a fall in *Sdad1*, leaving the transcript levels of the remaining five hub genes unchanged.

● **CONCLUSION:** These findings identify *Stat3* as a point of convergence between RNA modification, immune dysregulation, and angiogenesis, nominating the hub genes as candidate biomarkers and the associated drug–gene interactions as repurposing leads.

● **KEYWORDS:** diabetic retinopathy; angiogenesis; RNA modification; biomarkers; therapeutic targets

DOI:10.18240/ijo.2026.10.05

Citation: Wang X, Wu DP, Du W, Li R, Lou W, Chen RR, Liao YJ, Li Q, Li XM, Cui HP, Zhang JL. Angiogenesis-RNA modification in diabetic retinopathy: biomarkers and targets. *Int J Ophthalmol* 2026;19(10):1914-1928

INTRODUCTION

Among working-age adults worldwide, diabetic retinopathy (DR) ranks as a major cause of visual

impairment, with vision loss arising mainly from diabetic macular edema (DME) and proliferative DR (PDR). The burden is set to deepen as diabetes becomes more prevalent: by 2045, an estimated 700 million adults will be living with diabetes, approximately 160.5 million of whom are projected to have DR[1]. The advanced form of the disease, PDR, is defined by hypoxia-driven neovascularization at the vitreoretinal interface and often complicated by vitreous hemorrhage and tractional retinal detachment. Although metabolic, immune, and inflammatory pathways are known to interact in its pathogenesis, the precise mechanisms have yet to be fully worked out[2]. Current management still rests on retinal photocoagulation and intravitreal anti-vascular endothelial growth factor (VEGF) agents, yet their clinical utility is bounded by uneven responsiveness across patients, complications such as permanent loss of the peripheral visual field and aggravation of macular edema, and the absence of any capacity to restore damage already present[3]. Addressing these unmet clinical needs requires a more complete characterization of DR pathogenesis, which would in turn facilitate the development of targeted therapies.

Evidence linking DR to epigenetic mechanisms continues to accumulate: changes in DNA methylation, histone modification patterns, and non-coding RNA-mediated gene regulation, all acting independently of DNA sequence, have each been tied to disease initiation and advancement[4]. Beyond these epigenetic mechanisms lies a further tier of post-transcriptional control: chemical modification of RNA bases, in which methyl groups added at specific positions produce marks such as N6-methyladenosine (m^6A), N1-methyladenosine (m^1A), 5-methylcytosine (m^5C), and 7-methylguanosine (m^7G), each steering nuclear export, transcript stability, and translational output[5]. Properly balanced, these modifications sustain cell survival, proliferation, and migration. Their disturbance, by contrast, tracks with aging, tumorigenesis, and stress responses, promotes angiogenesis, and has been documented in age-related macular degeneration (AMD), DR, cataract, glaucoma, and myopia[6]. Among these marks, m^6A has been characterized in the greatest depth. Its installation rests with methyltransferase "writers" such as methyltransferase-like 3 (METTL3), removal is carried out by the demethylases fat mass and obesity-associated protein (FTO) and alkB homolog 5 (ALKBH5), and interpretation falls to YTH domain family proteins, the "readers" that recognize the modified bases[7] . Corneal neovascularization is a ocular process in which m^6A has been implicated[8], and Bai *et al*[9] showed that FTO inhibitors suppress VEGF release and choroidal neovascularization, suggesting FTO inhibition as a potential strategy for neovascular AMD, PDR, retinal vein occlusion, and retinopathy of prematurity. Although these findings implicate RNA modifications in ocular neovascularization, their functions, regulatory mechanisms, and value as biomarkers or therapeutic targets in DR-associated angiogenesis remain to be in-depth explored.

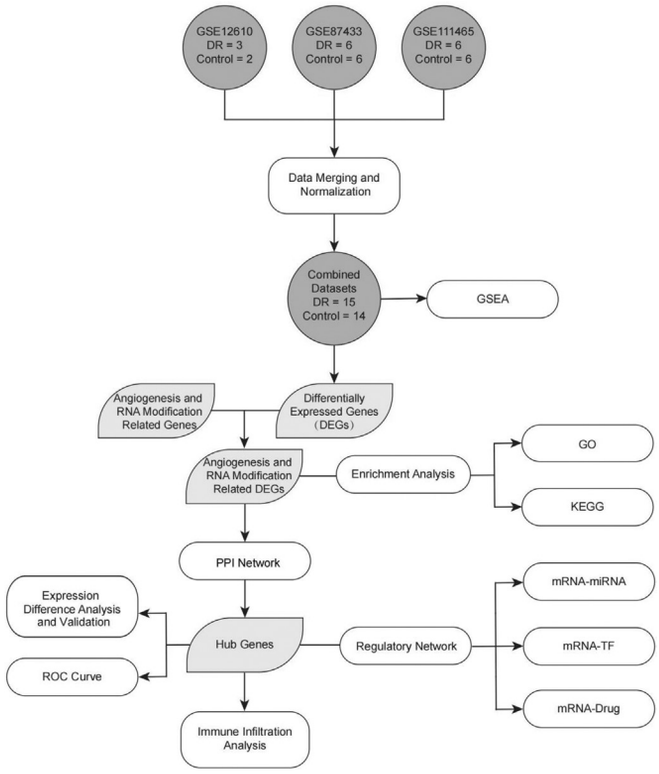

Figure 1 Overall study design DR: Diabetic retinopathy; DEGs: Differentially expressed genes; GO: Gene Ontology; GSE: Gene Expression Omnibus Series; GSEA: Gene Set Enrichment Analysis; KEGG: Kyoto Encyclopedia of Genes and Genomes; PPI: Protein-protein interaction; ROC: Receiver operating characteristic curve; TF: Transcription factor.

To address this gap, our study set out to identify angiogenesis-related targets governed by RNA modifications in DR, combining bioinformatic discovery with experimental verification to nominate candidate biomarkers and therapeutic targets.

MATERIALS AND METHODS

Ethical Approval Sprague-Dawley rats aged 5–6wk were obtained from the Shanghai Laboratory Animal Research Center (license number: SCXK 2021–0002) and kept under routine laboratory housing. Handling was carried out by experienced staff, with every effort made to limit animal distress. The Animal Ethics Committee approved all experimental procedures (approval number: 2023-DWYY-53JZS), and the work followed the 3R principles of Replacement, Reduction, and Refinement.

Data Sources and Preprocessing The overall analytical pipeline is depicted in Figure 1. In this study, a keyword-based search of Gene Expression Omnibus (GEO) was performed with the terms "Diabetic Retinopathy" and "Retina". Datasets

Table 1 Overview of the three GEO datasets used in this study

Parameters	GSE12610	GSE87433	GSE111465
Platform	GPL1261	GPL20710	GPL20710
Species	Mus musculus	Mus musculus	Mus musculus
Tissue	Retina	Retina	Retina
Samples in DR group	3	6	6
Samples in Control group	2	6	6
Reference	-	PMID: 28321468	-

DR: Diabetic retinopathy; GEO: Gene Expression Omnibus; GPL: Gene Expression Omnibus Platform; GSE: Gene Expression Omnibus Series.

were eligible if the samples were derived from retinal tissue, the grouping of DR and control subjects was explicitly defined, and complete expression profiles were available. Ultimately, GSE12610, GSE87433, and GSE111465 were retained for subsequent analysis[10-11]. GSE12610 was generated on the GPL1261 platform, whereas GSE87433 and GSE111465 were based on GPL20710 (Table 1). Using the platform-specific annotation files, probes were collapsed to gene-level expression values in each dataset. Probes lacking annotation or detectable signals were discarded, and genes covered by multiple probes were represented by their mean value. Each dataset was normalized with the normalizeBetweenArrays function of the limma package to attenuate technical variation before integration[12]. Only genes measurable in all three datasets were retained for integration, yielding a combined matrix comprising 15 DR samples and 14 control samples[13]. ComBat (sva package) removed residual batch effects attributable to dataset origin, and the outcome of the correction was inspected through boxplots of expression distributions and principal component analysis (PCA).

We assembled the angiogenesis-related genes (ARGs) from two sources. GeneCards was queried with the term "Angiogenesis" to screen for ARGs, and protein-coding genes with relevance scores exceeding 3 were retained. This threshold reduced background noise while capturing a core of 688[14-15]. A Molecular Signatures Database (MSigDB) search using the same keyword returned the gene set "GOBP_REGULATION_OF_CELL_MIGRATION_INVOLVED_IN_ANGIOGENESIS", which comprises 39 ARGs. After merging and deduplication, a total of 700 ARGs were compiled, and 676 ARGs were obtained after conversion to mouse orthologs with the R package homologene. RNA modification-related genes (RMRGs) were compiled from GeneCards and the literature. GeneCards was queried with "RNA Modification" for protein-coding entries (412 genes), and 76 additional genes were manually curated from PubMed literature for "m^1A", "m^5C", "m^6A", and "m^7G"[16-17]. After merging and deduplication, 459 RMRGs were retained, and 418 remained after ortholog mapping to mouse genes.

Differential Expression and Enrichment Analysis After the datasets were merged, samples were assigned to DR and control cohorts. Differential expression was called in the limma package under two criteria, |log fold change (FC)|>0 and adjusted P<0.05, with positive logFC values indicating up-regulation and negative values down-regulation. Differentially expressed angiogenesis- and RNA modification-related genes (A&RMRGs) were defined as the overlap among the differentially expressed genes (DEGs), ARGs, and RMRGs, and are illustrated in a Venn diagram.

Functional annotation of the differentially expressed A&RMRGs relied on Gene Ontology (GO) and Kyoto Encyclopedia of Genes and Genomes (KEGG) pathway enrichment implemented in the clusterProfiler R package[18]. GO terms were assessed separately for the biological process (BP), cellular component (CC), and molecular function (MF) categories[19-20]. The Benjamini-Hochberg (BH) correction was applied to raw P values, and enriched terms with adjusted P<0.05 and false discovery rate (FDR, Q value) below 0.05 were regarded as significant.

For the combined datasets, Gene Set Enrichment Analysis (GSEA) was run on the entire gene list ordered by logFC to detect enrichment patterns tied to the phenotype[21]. Running within the clusterProfiler R package, the analysis used a random seed of 2020, 5000 permutations, and a gene-set size range of 10–500 members. The curated canonical pathway collection ("m2.all.v2023.2.Mm.symbols.gmt", MSigDB) were tested, and results with an adjusted P below 0.05 were deemed significant[22].

PPI and Hub Gene Selection Protein-protein interactions (PPI) among the differentially expressed A&RMRGs were mapped with the STRING database, setting the minimum required interaction score at 0.400[23]. Five algorithms of the Cytoscape plugin cytoHubba were applied to score node importance: maximal clique centrality (MCC), degree, maximum neighborhood component (MNC), edge percolated component (EPC), and closeness[24-26]. Hub genes were defined as those shared across the five ranked lists, with the overlap displayed in a Venn diagram.

Comparison plots illustrated how hub gene expression differed between DR and control samples. To determine whether each gene could discriminate DR samples from controls, we constructed receiver operating characteristic (ROC) curves

with the pROC package. The area under the curve (AUC) served as the measure of diagnostic performance. Following conventional interpretation, AUCs between 0.5 and 0.7 denoted low accuracy, those between 0.7 and 0.9 moderate accuracy, and values above 0.9 high accuracy.

Immune Infiltration Analysis Infiltration by 28 immune cell subpopulations, including activated B cells and $CD4^+$ and $CD8^+$ T cells, was profiled in each sample by single-sample gene set enrichment analysis (ssGSEA) carried out in the gene set variation analysis (GSVA) package; for each cell type, the enrichment score provided an estimate of its infiltration level[27-28]. The two groups were then compared for every cell type, and only subpopulations showing significant between-group differences (P<0.05) were retained when building the immune infiltration matrix. Differences in infiltration across groups were visualized in grouped comparison plots, while associations between the infiltrating immune cells and hub genes were examined in a heatmap built with pheatmap. The strength of each correlation was rated as negligible when the absolute coefficient was below 0.3, weak at 0.3–<0.5, moderate at 0.5–<0.8, and strong above 0.8.

Regulatory Network Construction We next set out to characterize the upstream regulation of the hub genes through three networks. The first of these, a hub gene–miRNA network, drew on MicroRNA Target Prediction Database (miRDB): miRNAs with predicted binding sites in the hub genes were retrieved from the database and their interactions with the genes displayed in Cytoscape[29]. A hub gene-transcriptional regulators (TFs) network was then derived from ChIPBase, which catalogs TFs with predicted binding to the promoters or enhancers of these genes[30]. To explore therapeutic options, we queried the Comparative Toxicogenomics Database (CTD) for drugs with reported interactions involving the hub genes; the retrieved gene–drug associations were then compiled into the third network, a hub gene–drug map[31]. All networks were visualized and integrated within Cytoscape.

Validation in rRMECs For rat retinal microvascular endothelial cells (rRMECs) isolation, dissected retinas were incubated in collagenase type IV plus DNase I at 37°C for 45min. The resulting suspension was passed through a 40 μm filter, and the trapped microvessel fragments were released by a 10min exposure to 0.1% trypsin-ethylenediaminetetraacetic acid (EDTA). After resuspension in endothelial cell growth medium (EGM)-2 microvascular (MV), the vessel fragments were seeded into fibronectin-coated plates and incubated at 37°C in a humidified 5% CO_2 atmosphere. The endothelial population was then isolated by immunomagnetic CD31 selection. Flow cytometry verified that purity reached 95% or higher, and von Willebrand factor immunoreactivity confirmed the endothelial phenotype. The validated rRMECs were thereafter grown in Dulbecco's Modified Eagle Medium (DMEM) supplemented with 10% fetal bovine serum (Gibco) and 1% penicillin-streptomycin (Invitrogen). The high-glucose challenge consisted of 48h of exposure to 30 mmol/L D-glucose (Sigma-Aldrich), cells incubated at 5.5 mmol/L D-glucose under otherwise identical conditions constituted the normoglycemic reference group. For gene expression analysis, total RNA prepared from rRMECs with TRIzol (Beyotime Biotechnology) was reverse-transcribed using PrimeScript™ RT Master Mix (Takara), with cDNA synthesis conducted at 37°C for 15min followed by enzyme inactivation at 85°C for 5s. Quantitative polymerase chain reaction (qPCR) reactions, each performed in triplicate on a QuantStudio 6 platform (Thermo Fisher Scientific) with TB Green® Premix Ex Taq™ II (Takara), were initiated by 30s of denaturation at 95°C and completed over 40 cycles of 95°C (5s) and 60°C (30s). Fold changes in gene expression, computed by the $2^{-\Delta\Delta Ct}$ method with *Actb* as the reference gene, were derived from three biological replicates analyzed per experimental group.

Statistical Analysis We conducted all analyses in R 4.2.2. Unless the Shapiro-Wilk test indicated non-normality or Levene's test detected heteroscedasticity, data were reported as mean±standard deviation (SD). Otherwise, medians with interquartile ranges were used. Depending on data distribution, pairwise differences were tested with an unpaired two-tailed *t*-test or its non-parametric counterpart, the Wilcoxon rank-sum test. Comparisons spanning multiple groups relied on one-way analysis of variance (ANOVA) with Tukey's/Bonferroni post hoc test or, alternatively, the Kruskal-Wallis *H* test with Dunn's correction. Spearman's rank correlation coefficients were computed to quantify monotonic associations between variables, with statistical significance defined as P<0.05.

RESULTS

Merging of DR Datasets To integrate the GEO series GSE12610, GSE111465, and GSE87433 into one analysis, we first collapsed them into a common expression matrix and then applied ComBat (sva R package) to strip out batch effects introduced by the individual series. Boxplots of the expression distributions and PCA plots of the integrated dataset are shown before and after correction in Figure 2. Following ComBat adjustment, samples from the three series were no longer separated by batch.

Differential Expression of A&RMRGs in Diabetic Retina In total, 584 genes met the differential expression criteria in DR relative to control retinas, with an even split of 292 upregulated and 292 downregulated genes (Figure 3A). Intersecting this list with the ARG and RMRG collections yielded 42 differentially expressed A&RMRGs: *Stat3*, *Pros1*, *Trdmt1*, *Plxnc1*, *Hspa2*, *Smad2*, *Hspa9*, *Srsf9*, *Map3k3*, *Nsun4*,

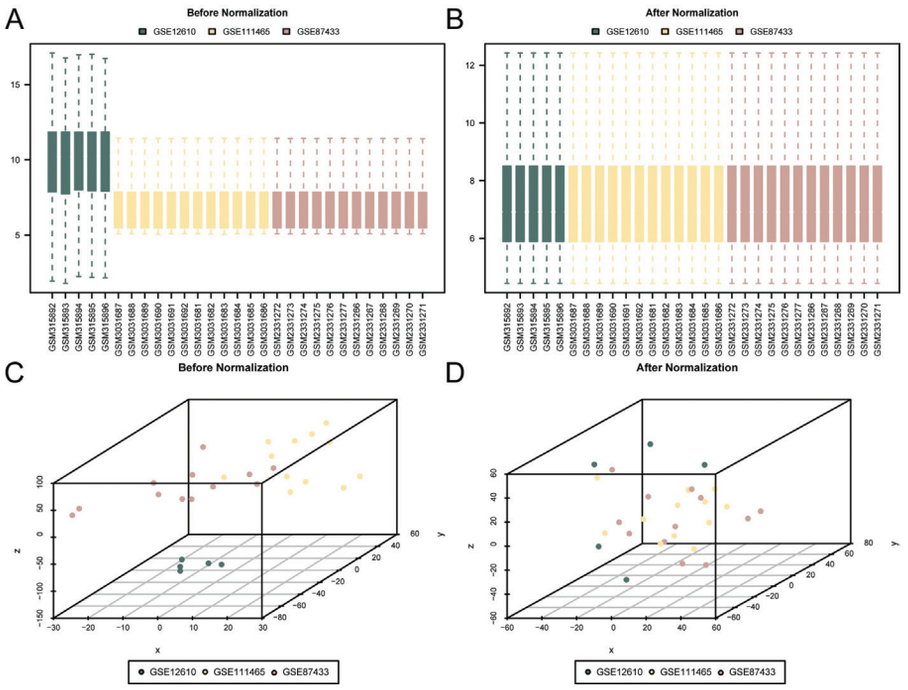

Figure 2 Assessment of batch effects in the combined DR datase A–B: Expression distribution boxplots; C–D: Three-dimensional PCA plots of the integrated GEO datasets; A, C: Before batch effect correction; B, D: After batch effect correction. GEO: Gene Expression Omnibus; GSE: Gene Expression Omnibus Series; PCA: Principal component analysis; DR: Diabetic retinopathy.

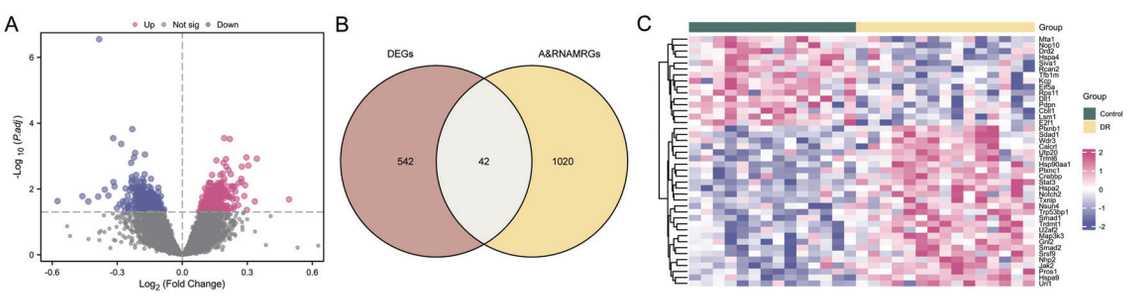

Figure 3 Identification of DEGs and differentially expressed A&RMRGs in the combined DR dataset A: Volcano plot of DEGs between DR and control samples; B: Venn diagram in which the DEGs list was intersected with the ARG and RMRG collections to extract the differentially expressed A&RMRGs; C: Heatmap of differentially expressed A&RMRGs expression in DR versus control samples. A&RMRGs: Angiogenesis- and RNA modification-related genes; DR: Diabetic retinopathy; DEGs: Differentially expressed genes.

Sdad1, *Hsp90aa1*, *Utp20*, *Uri1*, *Smad1*, *Gnl2*, *Wdr3*, *Crebbp*, *Trp53bp1*, *Calcrl*, *Notch2*, *Nhp2*, *U2af2*, *Trmt6*, *Txnip*, *Jak2*, *Plxnb1*, *Lsm1*, *E2f1*, *Drd2*, *Siva1*, *Nop10*, *Mta1*, *Eif5a*, *Tfb1m*, *Dll1*, *Rps11*, *Kcp*, *Hspa4*, *Rcan2*, *Pdpn*, *Cbll1* (Figure 3B). The expression of these genes across the two groups is presented as a heatmap (pheatmap R package; Figure 3C).

GO and KEGG Enrichment Analysis GO analysis of the 42 differentially expressed A&RMRGs returned RNA modification, non-coding RNA processing, and ribonucleoprotein complex biogenesis as the dominant BP. Enrichment was strongest in the CC domain for the RNA polymerase II complex, SMAD complex, and 90S preribosome. At the MF level, RNA polymerase II transcription factor binding and snoRNA binding were significantly over-represented (Table 2). Pathway-level analysis (KEGG) highlighted three dominant themes among these genes: chemical carcinogenesis-receptor activation, Th17 differentiation, and Notch signaling. Bubble plots, cluster plots, and enrichment map (EMAP) networks depicting these results are presented in Figure 4. The differentially expressed A&RMRGs were mainly enriched in RNA processing machinery, inflammatory immune regulation, cellular stress, and angiogenesis. The shared focus of the enriched categories points to immune dysfunction and post-transcriptional regulation as contributors to DR development.

Gene Set Enrichment Analysis When the analysis was extended to the entire ranked gene list, GSEA identified 23 significantly enriched gene sets, of which 7 were upregulated and 16 downregulated (Table 3). Figure 5 displays the three most prominent gene sets in each direction. Of these, triglyceride catabolism [normalized enrichment score (NES)=2.00] was represented solely by the fatty acid-binding

Table 2 GO terms and KEGG pathways enriched among differentially expressed A&RMRGs

Ontology	ID	Description	GeneRatio	BgRatio	*P*	*P*.adjust	*Q*
BP	GO:0009451	RNA modification	7/42	144/28814	1.57E-09	2.6E-06	1.52E-06
BP	GO:0034470	ncRNA processing	9/42	393/28814	4.47E-09	3.28E-06	1.92E-06
BP	GO:0022613	Ribonucleoprotein complex biogenesis	9/42	406/28814	5.93E-09	3.28E-06	1.92E-06
BP	GO:0042254	Ribosome biogenesis	8/42	299/28814	1.06E-08	4.42E-06	2.59E-06
BP	GO:0001510	RNA methylation	5/42	70/28814	5.8E-08	1.93E-05	1.13E-05
CC	GO:0090575	RNA polymerase II transcription regulator complex	5/42	235/28739	2.33E-05	0.003563	0.002598
CC	GO:0071141	SMAD protein complex	2/42	10/28739	9.31E-05	0.007124	0.005196
CC	GO:0043235	Receptor complex	5/42	423/28739	0.000367	0.018084	0.013188
CC	GO:0005697	Telomerase holoenzyme complex	2/42	22/28739	0.000473	0.018084	0.013188
CC	GO:0030686	90S preribosome	2/42	28/28739	0.000769	0.021052	0.015353
MF	GO:0061629	RNA polymerase II-specific DNA-binding transcription factor binding	8/40	377/28275	4.91E-08	7.57E-06	4.04E-06
MF	GO:0097718	Disordered domain specific binding	4/40	37/28275	2.19E-07	1.69E-05	9E-06
MF	GO:0048156	Tau protein binding	3/40	22/28275	3.96E-06	0.000204	0.000108
MF	GO:0030515	snoRNA binding	3/40	32/28275	1.26E-05	0.000487	0.00026
MF	GO:0044183	Protein folding chaperone	3/40	40/28275	2.5E-05	0.00077	0.00041
KEGG	mmu05207	Chemical carcinogenesis - receptor activation	6/30	225/9000	8.2E-05	0.008529	0.006043
KEGG	mmu04659	Th17 cell differentiation	4/30	105/9000	0.00038	0.01726	0.012229
KEGG	mmu03008	Ribosome biogenesis in eukaryotes	4/30	121/9000	0.00065	0.01726	0.012229
KEGG	mmu05417	Lipid and atherosclerosis	5/30	216/9000	0.000664	0.01726	0.012229
KEGG	mmu04330	Notch signaling pathway	3/30	60/9000	0.001006	0.019459	0.013787

A&RMRGs: Angiogenesis- and RNA modification-related genes; BP: Biological process; CC: Cellular component; GO: Gene Ontology; MF: Molecular function; KEGG: Kyoto Encyclopedia of Genes and Genomes.

Table 3 GSEA-identified gene sets significantly enriched in the combined DR dataset

ID	Set size	Enrichment score	NES	*P*	*P*.adjust	*Q*	Rank
REACTOME_TRIGLYCERIDE_CATABOLISM	10	0.808920128843375	1.99889708013999	0.000206703375099486	0.0268585198019895	0.0251987732933781	71
REACTOME_GENE_SILENCING_BY_RNA	40	0.550101420857544	1.97625775355934	0.000204528198694764	0.0268585198019895	0.0251987732933781	4158
REACTOME_TRANSPORT_OF_THE_SLBP_DEPENDANT_MATURE_MRNA	34	0.560107732605255	1.94637723507959	0.00027815544397606	0.0289142584013114	0.0271274756677705	3407
REACTOME_NUCLEAR_ENVELOPE_BREAKDOWN	46	0.521443499516473	1.91859751331401	0.000157938281435179	0.0235988024467179	0.0221404931185379	3407
RAMALHO_STEMNESS_UP	185	0.346640593569187	1.62664585042611	0.000158914494590693	0.0235988024467179	0.0221404931185379	3359
MONNIER_POSTRADIATION_TUMOR_ESCAPE_UP	381	0.314512588457013	1.60504030198859	1.00731190852719e-05	0.00418840291565607	0.00392957677158082	5084
LAZARO_GENETIC_MOUSE_MODEL_HIGH_GRADE_LARGE_CELL_NEUROENDOCRINE_LUNG_CARCINOMA_UP	357	0.310225746323422	1.57122024025064	4.25524854605085e-05	0.00982962414137747	0.00922219363255232	3722
REACTOME_NEURONAL_SYSTEM	309	-0.305681954	-1.676637638	0.000473364257547939	0.0427880126713985	0.0401438887522348	4763
YAO_TEMPORAL_RESPONSE_TO_PROGESTERONE_CLUSTER_13	150	-0.381229832	-1.703012085	0.000251936830090838	0.0289142584013114	0.0271274756677705	4929
REACTOME_MUSCLE_CONTRACTION	153	-0.387493182	-1.724268184	0.000113965626546653	0.0215395034173174	0.020208450334062	2667
REACTOME_GPCR_LIGAND_BINDING	330	-0.351714152	-1.733611618	1.07801302494695e-06	0.000747063026288235	0.000700897591307612	3788
MCCLUNG_CREB1_TARGETS_UP	93	-0.424561751	-1.745592645	0.000311214821863398	0.0296025403498945	0.027773224611202	2769
REACTOME_POTASSIUM_CHANNELS	87	-0.431280217	-1.762507861	0.000277680401419151	0.0289142584013114	0.0271274756677705	4807
MODY_HIPPOCAMPUS_POSTNATAL	55	-0.501644649	-1.881686975	0.000137221385673746	0.0235988024467179	0.0221404931185379	4252
REACTOME_RESPIRATORY_ELECTRON_TRANSPORT_ATP_SYNTHESIS_BY_CHEMIOSMOTIC_COUPLING_AND_HEAT_PRODUCTION_BY_UNCOUPLING_PROTEINS	92	-0.456413957	-1.888045716	2.11641130380496e-05	0.00574391346585124	0.00538896314129888	3545
JIANG_AGING_CEREBRAL_CORTEX_DN	44	-0.538856969	-1.939681595	0.000313254395236979	0.0296025403498945	0.027773224611202	4056
STARK_PREFRONTAL_CORTEX_22Q11_DELETION_DN	461	-0.38561069	-1.946001162	1e-10	2.079e-07	1.95052631578947e-07	3144
REACTOME_COMPLEX_I_BIOGENESIS	45	-0.53972173	-1.955041603	0.000227791302631657	0.0278575363630127	0.0261360547230007	3745
REACTOME_RESPIRATORY_ELECTRON_TRANSPORT	76	-0.488187979	-1.959992567	1.59060270967225e-05	0.00551143838901434	0.00517085407196961	3095
WP_ELECTRON_TRANSPORT_CHAIN	68	-0.510796917	-2.019963186	2.21026011191967e-05	0.00574391346585124	0.00538896314129888	3545
REACTOME_THE_CANONICAL_RETINOID_CYCLE_IN_RODS_TWILIGHT_VISION	19	-0.711201086	-2.098351533	5.37353736821221e-05	0.0111715841885132	0.010481226045576	33
LEIN_NEURON_MARKERS	62	-0.548781525	-2.132447902	2.46731833669076e-06	0.00128238870549502	0.00120314233628631	3567
LEE_TARGETS_OF_PTCH1_AND_SUFU_DN	85	-0.539976293	-2.197318061	1.22968079458471e-07	0.00012782531859708	0.000119926237492919	3163

DR: Diabetic retinopathy; Q: False discovery rate; GSEA: Gene Set Enrichment Analysis; NES: Normalized enrichment score.

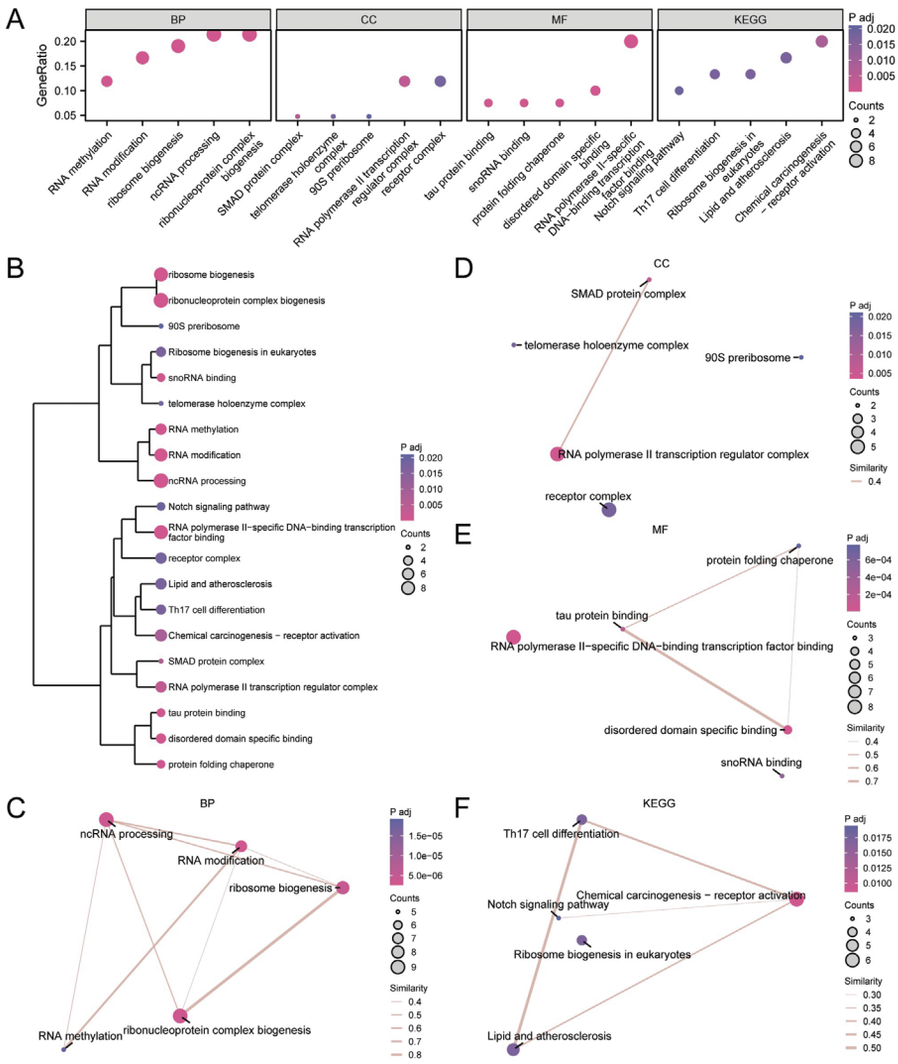

Figure 4 Functional enrichment profiles of the differentially expressed A&RMRGs A: Bubble plot displaying enriched GO terms across the BP, CC, and MF categories together with KEGG pathways; B: Cluster plot grouping the enriched terms and pathways; C–F: EMAP networks visualizing term-to-term similarity for BP (C), CC (D), MF (E), and KEGG (F) results, with node size proportional to molecule count and edge thickness to the strength of pairwise similarity. Significance thresholds were adjusted $P<0.05$ and Q value<0.25 (Benjamini-Hochberg correction). A&RMRGs: Angiogenesis- and RNA modification-related genes; BP: Biological process; CC: Cellular component; EMAP: Enrichment map; GO: Gene Ontology; MF: Molecular function; KEGG: Kyoto Encyclopedia of Genes and Genomes.

protein genes Fabp4, Fabp7, and Fabp9 (Figure 5B), whereas gene silencing by RNA (NES=1.97) had a leading edge consisting of *Ago1–Ago4* and *Tnrc6b* (Figure 5C). Stem-loop binding protein (SLBP)-dependent mature mRNA transport (NES=1.93) occupied the third position (Figure 5D). Neuronal identity dominated the downregulated fraction. Targets of *Ptch1* and *Sufu* (NES=-2.20) carried *Gad1*, *Slc32a1*, *Vamp2*, *Rab3a*, *Nefh*, and *Thy1* among their core genes (Figure 5E), accompanied by Lein neuron markers (NES=-2.12; Figure 5F) and by the canonical retinoid cycle in rods (NES=-2.10), for which Rpe65, Rdh5, Lrat, and Rlbp1 accounted for the enrichment (Figure 5G). Overall, the diabetic retina coupled activation of lipid-handling and post-transcriptional regulatory programs with attenuation of programs governing neuronal identity and visual function.

Network Construction and Hub Gene Screening In the STRING PPI network of the 42 differentially expressed A&RMRGs, 30 genes formed connected interactions (Figure 6A). Five algorithms implemented in cytoHubba (MCC, degree, MNC, EPC, and closeness) were used to rank these nodes, and the resulting top 10 lists were plotted as subnetworks in which node color was graded from red to yellow in descending order of score (Figure 6B–6F). Seven genes appeared in all five lists and were identified as the hub genes, they were *Wdr3*, *Crebbp, Sdad1*, *Stat3*, *Gnl2*, *Nhp2,* and *Hsp90aa1* (Figure 6G).

Immune Landscape of DR and Its Links to Hub Genes Applying ssGSEA to the merged dataset, we profiled the infiltration of 28 immune cell types and detected significant between-group differences in four of them: central memory

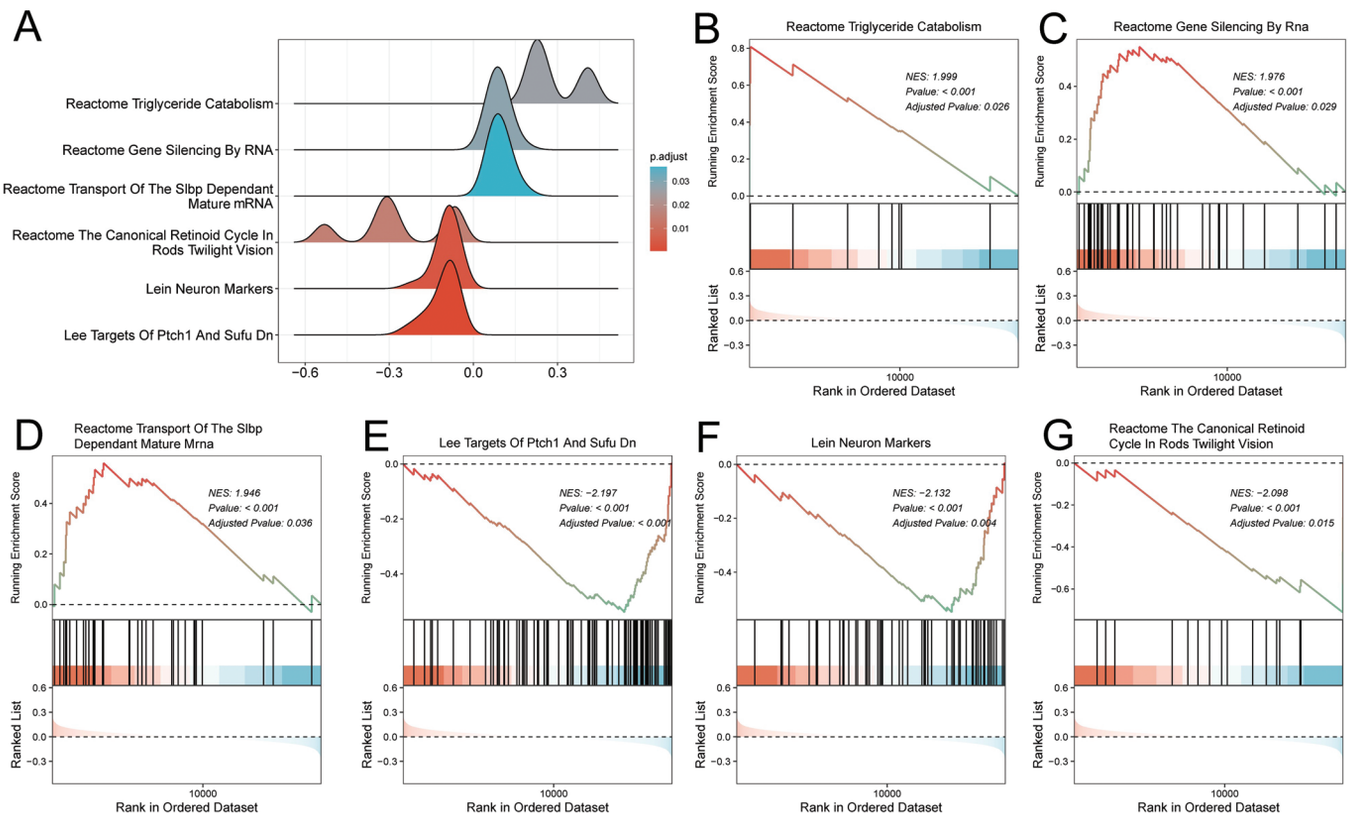

Figure 5 Significantly enriched gene sets identified by GSEA in the combined DR dataset A: Ridge plot showing the normalized enrichment scores of the three most strongly up-regulated and down-regulated gene sets. B–G: Enrichment plots of the six gene sets with the largest absolute NES values in each direction. The three most strongly up-regulated gene sets: triglyceride catabolism (B), gene silencing by RNA (C), and Slbp-dependent mature mRNA transport (D), and the three most strongly down-regulated gene sets: Lee targets of PTCH1 and SUFU (E), Lein neuron markers (F), and the canonical retinoid cycle in rods (G). Significance was defined as adjusted P<0.05 and FDR Q value<0.25 (Benjamini-Hochberg correction). NES: Normalized enrichment score; FDR: False discovery rate; GSEA: Gene Set Enrichment Analysis; DR: Diabetic retinopathy.

CD8$^+$ T cells were elevated in DR (P<0.001), while monocytes (P<0.01), Tregs (P<0.05), and CD56^{bright} natural killer (NK) cells (P<0.05) were diminished (Figure 7A). Within the correlation matrix of the four cell types (Figure 7B), monocytes and central memory CD8$^+$ T cells showed the most pronounced negative coupling (r=-0.439), and Tregs with CD56^{bright} NK cells the most pronounced positive coupling (r=0.341). Of the hub genes, Nhp2 rose in step with central memory CD8$^+$ T cells (r=0.539, P=0.003), whereas Stat3 moved oppositely to monocytes (r=-0.604, P<0.001; Figure 7C–7E). Together, these results indicate that the altered immune cell composition of the DR retina may fuel inflammatory responses and aberrant angiogenesis, underscoring immune dysregulation as a central feature of DR pathogenesis.

Hub Gene Regulatory Networks at miRNA, Transcription Factor, and Drug Levels Three databases were queried to construct regulatory networks around the hub genes. The upstream and pharmacological regulation of the hub genes is summarized in Figure 8. Target prediction in miRDB connected five of the seven hub genes with 60 miRNAs (Figure 8A), whereas ChIPBase documented 43 TFs acting on six of them (Figure 8B). On the therapeutic side, the CTD linked five hub genes to 47 drugs, in which quercetin also emerged from our drug prediction (Figure 8C).

Expression Changes and Diagnostic Value of the Hub Genes in DR Every one of the seven hub genes was significantly upregulated in DR retinas relative to controls (Wilcoxon rank-sum test, P<0.001; Figure 9A), and each discriminated DR from controls with an AUC of 0.848-0.964 (Figure 9B–9H). Diagnostic accuracy was high for *Stat3* (AUC=0.964, 95%CI: 0.892–1.000; Figure 9E) and *Gnl2* (AUC=0.914, 95%CI: 0.810–1.000; Figure 9D) and moderate for the other five genes, whose AUCs ranged from 0.848 (*Wdr3,* 95%CI: 0.700-0.995) to 0.881 (*Hsp90aa1*, 95%CI: 0.762–1.000; *Sdad1*, AUC=0.871, 95%CI: 0.725–1.000; *Nhp2*, AUC=0.862, 95%CI: 0.717–1.000; *Crebbp*, AUC=0.871, 95%CI: 0.737–1.000; all P<0.05).

Validation of Hub Genes Expression of the seven hub genes was quantified by reverse transcription quantitative polymerase chain reaction (RT-qPCR) in cultured rRMECs,

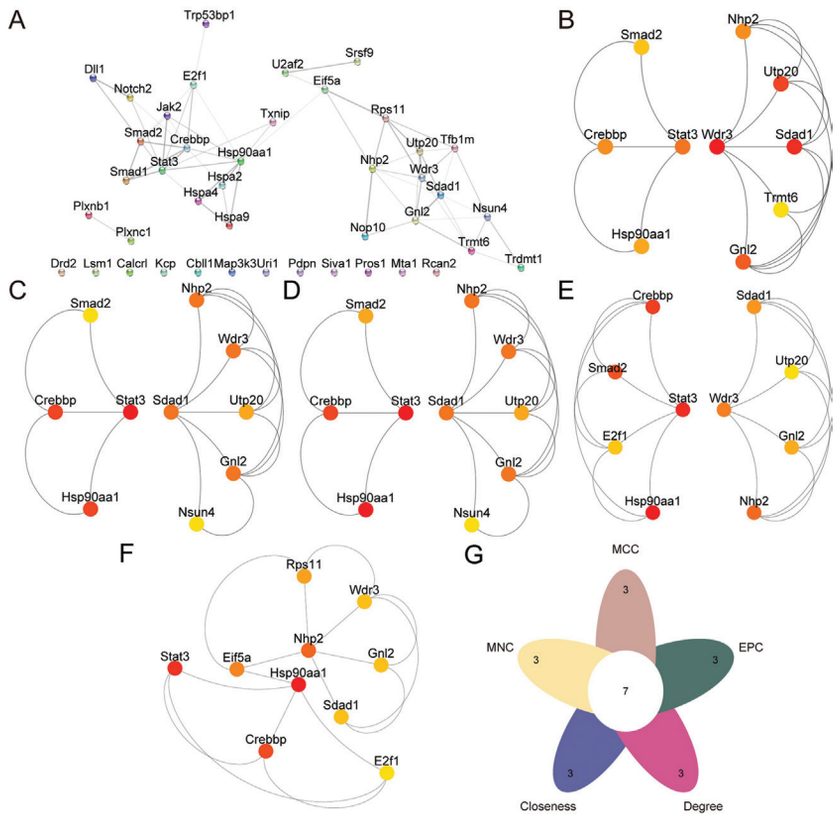

Figure 6 Hub gene selection among the differentially expressed A&RMRGs A: PPI network built in STRING from the differentially expressed A&RMRGs. B–F: Top 10 candidates highlighted by each of five cytoHubba ranking algorithms: B: MCC; C: MNC; D: Degree; E: EPC; F: Closeness. G: Venn diagram identifying the seven hub genes shared by all five algorithms. A&RMRGs: Angiogenesis- and RNA modification-related genes; EPC: Edge percolated component; MCC: Maximal clique centrality; MNC: Maximum neighborhood component; PPI: Protein-protein interaction; STRING: Search Tool for the Retrieval of Interacting Genes/proteins.

Table 4 Primers used for RT-qPCR analysis of the hub genes

Primer	Sequences (5'-3')
R-*Actb*-S	TGTCACCAACTGGGACGATA
R-*Actb*-A	GGGGTGTTGAAGGTCTCAAA
R-*Wdr3*-S	CTCCGAGAAAGGAATCTGCTAGTTA
R-*Wdr3*-A	TGAAACCAGAACCAAGCCC
R-*Crebbp*-S	CCAGGAGACTCATCAACACCC
R-*Crebbp*-A	TCATGACTTGAGCTTGCCCTT
R-*Sdad1*-S	GAACGATGCCAAAACTGTCAATG
R-*Sdad1*-A	GAAGAACGTCAAAGCAGCAACTAAT
R-*Stat3*-S	TTAACATTCTGGGCACGAACA
R-*Stat3*-A	TGACAATCAAGGAGGCATCAC
R-*Gnl2*-S	CGAGTGGAGCCGAATATTAAATG
R-*Gnl2*-A	CAAGAATGTGGACCTTTGCGTTA
R-*Nhp2*-S	ACAAGGGCGAGAAAGGGAT
R-*Nhp2*-A	CCAAGTCCGTCTTAGAGGGAATATA
R-*Hsp90aa1*-S	ATTTCCAACTCCTCAGACGCTC
R-*Hsp90aa1*-A	TTCGGTCTTGCTTGTTGGGA

RT-qPCR: Reverse transcription quantitative polymerase chain reaction; F: Forward primer; R: Reverse primer. All primers were designed for rat genes.

with the corresponding primer sequences provided in Table 4. Under high-glucose (HG, 30 mmol/L) conditions, *Stat3* was significantly upregulated (P<0.0001) and *Sdad1* significantly downregulated (P<0.0001) relative to the low-glucose (LG, 5.5 mmol/L) control, whereas *Wdr3*, *Crebbp*, *Gnl2*, *Nhp2*, and *Hsp90aa1* remained unchanged (P>0.05; Figure 10). *Stat3* was therefore the only hub gene whose upregulation in the DR retina was reproduced *in vitro*. However, the HG-induced decrease in *Sdad1*, opposite in direction to its retinal upregulation, suggests that factors in the retinal microenvironment beyond glucose alone drive its upregulation *in vivo*. These results point to *Stat3*, which operates at the interface of angiogenesis and inflammation, as a contributor to DR pathogenesis and a candidate therapeutic target.

DISCUSSION

Main Findings and Interpretation Integrating GEO datasets with *in vitro* validation, this study identified 42 differentially expressed A&RMRGs and seven upregulated hub genes in DR, with *Stat3* and *Gnl2* showing the highest diagnostic value. The diabetic retina combined activated RNA regulatory programs with an inflammatory shift and suppressed neuronal and visual-cycle programs, and only *Stat3* was confirmed in high-glucose-treated rRMECs. These findings nominate the hub genes as candidate biomarkers and position *Stat3* as a crass-talk point between RNA modification, immune dysregulation, and angiogenesis.

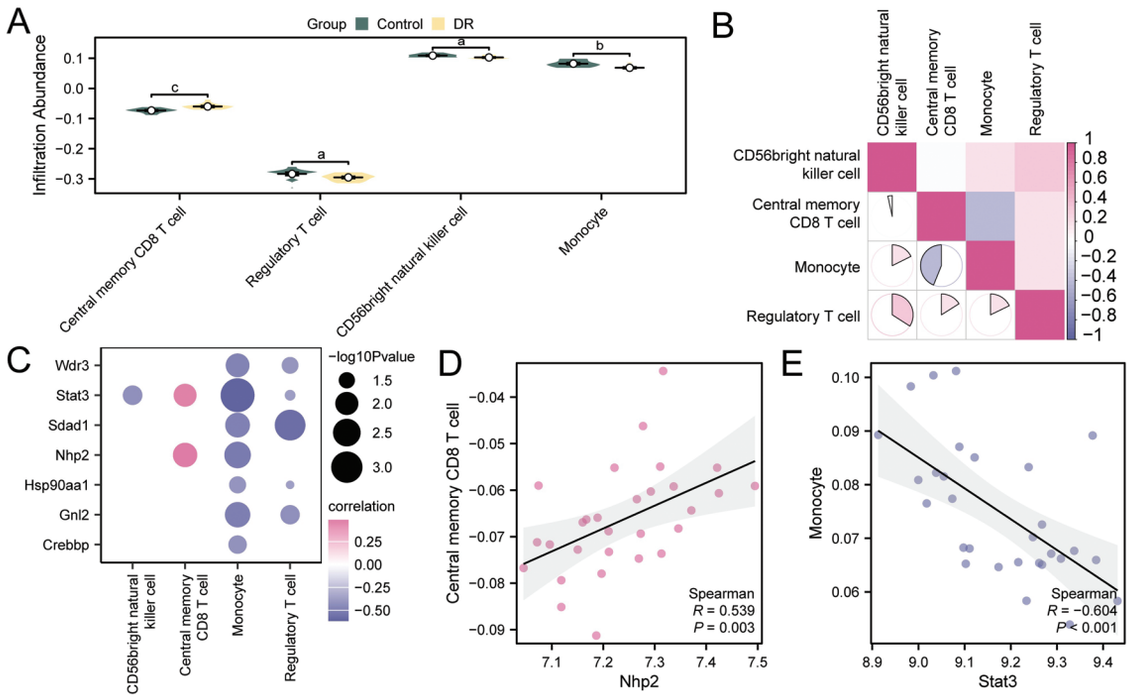

Figure 7 Immune infiltration changes in DR and their relationship to hub gene expression A: Grouped comparison of infiltrating immune cells in DR versus control samples (merged dataset; control, green; DR, yellow). B: Correlation heatmap of immune cell abundance, in which purple marks positive and blue marks negative associations. C: Correlations of each hub gene (x-axis) with the abundance of each immune cell type (y-axis), plotted as bubbles sized by *r*. D: Scatter plot of Nhp2 against central memory CD8$^+$ T cells (*r*=0.539, *P*=0.003). E: Scatter plot of Stat3 against monocytes (*r*=-0.604, *P*<0.001). DR: Diabetic retinopathy; ssGSEA: Single-sample gene-set enrichment analysis. [a]*P*<0.05, [b]*P*<0.01, [c]*P*<0.001.

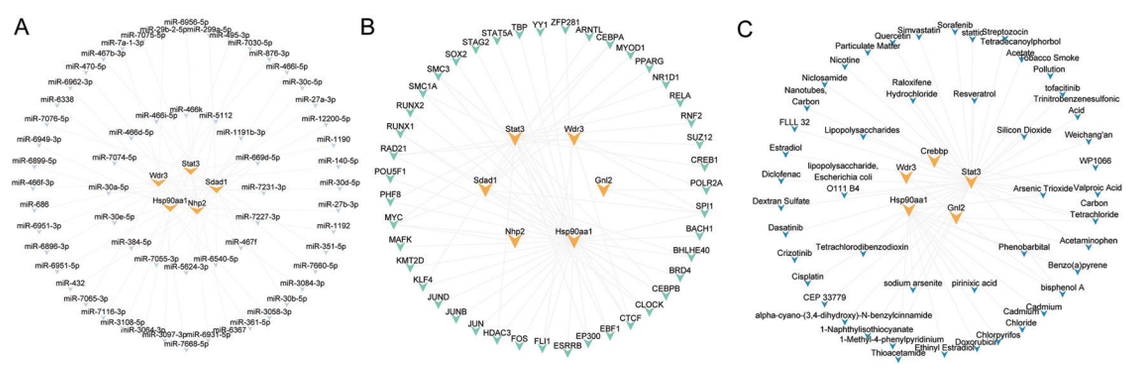

Figure 8 Upstream and pharmacological regulation of the hub genes A: Interactions between five hub genes and 60 miRNAs predicted by miRDB. B: Interactions between 6 hub genes and the 43 TFs recorded in ChIPBase. C: Interactions between 5 hub genes and 47 drugs documented in the CTD. CTD: Comparative Toxicogenomics Database; TFs: Transcription factors.

Taken together, targeted GO/KEGG analysis of the differentially expressed A&RMRGs and unbiased GSEA of them point to the same axis in DR, which enhanced post-transcriptional RNA regulation superimposed on a failing neuronal and visual-transduction program. Functionally, the hub genes participate in the same pathways identified by our analyses. Their reported roles span cell proliferation, ribosome biogenesis, cell cycle regulation, angiogenesis, telomere maintenance, tumor immunity, and stress responses, although most of this evidence comes from disease contexts other than DR, particularly cancer and cardiac disease. *Wdr3* promotes the growth of several malignant tumors and tracks with inflammatory mediators that decline under anti-inflammatory treatment[32-33]. Chen *et al*[34] reported that Sdad1 plays a key role in spinal cord injury, modulating microglial M1 polarization and the inflammatory response. Bioinformatic analysis by Dong *et al*[35] showed that G protein nucleolar 2 (GNL2), a ribosome biogenesis factor essential for unrestrained cancer growth, drives proliferation, migration, and invasion in hepatocellular carcinoma. CREB-binding lysine acetyltransferase (CREBBP), together with its paralog p300, acts as an acetyltransferase and transcriptional coactivator central to hematological malignancies and tumor immune responses[36]. Tao *et al*[37] found that *NHP2*, a RNA pseudouridylation-related gene, sustains the proliferation and

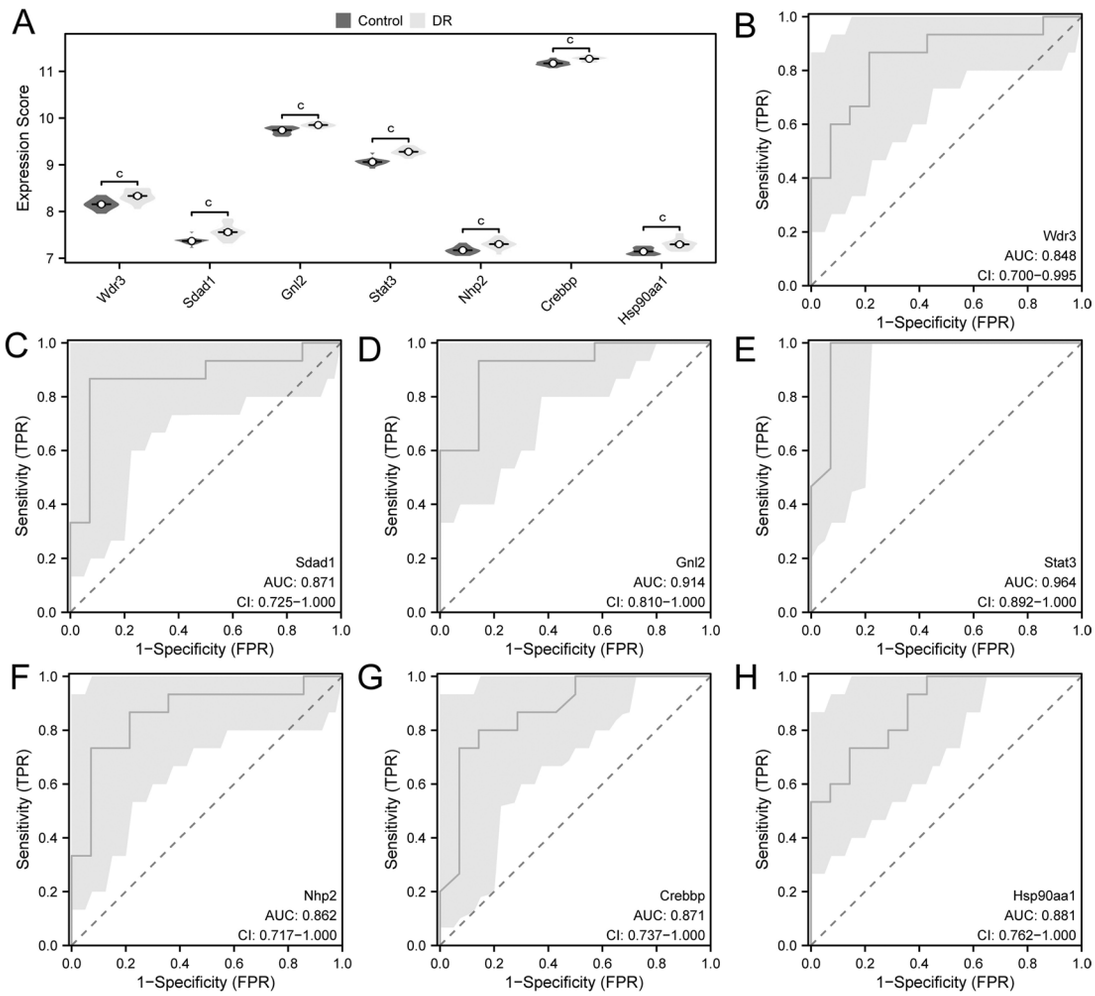

Figure 9 Evaluation of hub gene expression in DR and assessment of their diagnostic performance by ROC analysis A: Expression levels of the seven hub genes in DR versus control samples. B–H: ROC curves for each hub gene: *Wdr3* (B), *Sdad1* (C), *Gnl2* (D), *Stat3* (E), *Nhp2* (F), *Crebbp* (G), and *Hsp90aa1* (H). An AUC above 0.9 was considered indicative of high diagnostic performance, and an AUC of 0.7–0.9 of moderate performance. AUC: Area under the curve; CI: Confidence interval; DR: Diabetic retinopathy; FDR: False discovery rate; ROC: Receiver operating characteristic; TPR: True positive rate. ^{c}P<0.001.

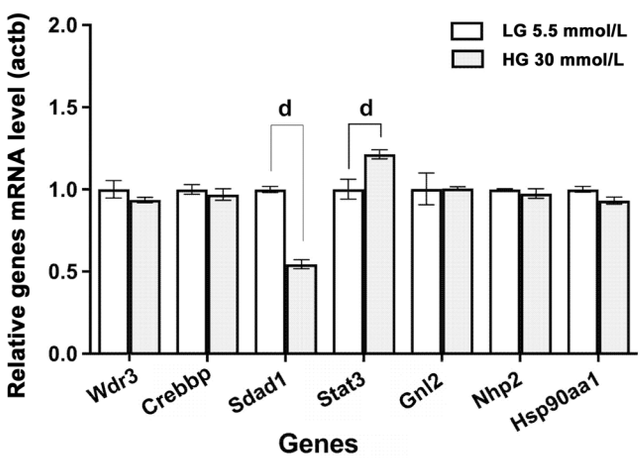

Figure 10 RT-qPCR analysis of hub gene expression in rRMECs Expression of the seven hub genes in rRMECs cultured under LG (5.5 mmol/L) or HG (30 mmol/L) conditions, normalized to *Actb*: *Wdr3*, *Sdad1*, *Gnl2*, *Stat3*, *Nhp2*, *Crebbp*, and *Hsp90aa1*. LG: Low glucose (5.5 mmol/L); HG: High glucose (30 mmol/L); rRMECs: Rat retinal microvascular endothelial cells. ^{d}P<0.0001.

invasiveness of uveal melanoma cells. More directly relevant to the eye, Yang *et al*[38] showed that reduced HSP90AA1 expression in retinal and fibrovascular membrane samples from PDR patients linked to altered splicing of cyclin H. In addition, Yan *et al*[39] demonstrated that its downregulation may induce the Müller cell proliferation associated with DR by simultaneously inhibiting necroptosis and activating mitogen-activated protein kinase signaling. Fang *et al*[40] reported that signal-induced proliferation-associated protein 1 (SIPA1) supports retinal angiogenic activity through signal transducer and activator of transcription 3 (STAT3) activation and the consequent regulation of VEGF release from Müller cells. Despite these mechanistic links and the significant AUCs observed in our ROC analysis, the clinical diagnostic value of these genes in DR remains largely untested, and future work will assess their expression and RNA modification status in peripheral blood, vitreous and aqueous humor, and epiretinal membranes from patients with DR.

In vitro, *Stat3* alone matched the bioinformatic prediction. RT-qPCR showed elevated *Stat3* expression under high glucose conditions, consistent with previous reports[41]. STAT3 activates VEGF transcription, and oxidative stress-induced STAT3 activation raises p-STAT3/VEGF levels to drive diabetic retinal neovascularization (RNV)[42-43], which explains why STAT3 inhibition improves visual function in diabetic rats[44]. Zhao *et al*[41] additionally reported that intravitreal graphene quantum dots suppressed neovascularization together with p-STAT3/periostin signaling in oxygen-induced retinopathy. STAT3 also upregulates WT1-associated protein (WTAP), which enhances the nuclear localization and methyltransferase activity of METTL3, forming a METTL3-STAT3 feedback loop that promotes liver cancer progression[45]. Empirical evidence linking RNA methylation to STAT3-mediated angiogenesis in DR remains insufficient and warrants further investigation.

The remaining hub genes deviated from prediction *in vitro*, among which five were unchanged and *Sdad1* moved opposite to its retinal pattern. Several factors may account for this. On the one hand, the bioinformatic predictions were derived from mouse retinal tissue, while the *in vitro* experiments used rRMECs, so species differences likely contribute. On the other hand, although high-glucose stimulation mimics the diabetic microenvironment, it cannot fully recapitulate the complex metabolic and inflammatory conditions *in vivo*. Furthermore, some genes may be regulated by post-transcriptional modification or translational control, such that changes in their mRNA levels do not necessarily directly reflect functional activity.

Role of Immune Dysregulation in DR Retinal immune privilege rests on the blood-retinal barrier and a local immunosuppressive milieu[46], and this privilege erodes in DR. Animal models of RNV have repeatedly shown activation of innate immune pathways, while in patients with DR, $CD8^+$ T cells accumulate in the vitreous[47]. Meng *et al*[48] found more helper T cells and M1/M2 macrophages but fewer plasma cells, NK cells, and mast cells in PDR. In oxygen-induced retinopathy, inhibition of M2 polarization attenuates RNV[49]. Mechanistically, diabetes and hypoxia enhance the recruitment of circulating $CD8^+$ T cells into the retina[50]. These cells express CXCR3, secrete inflammatory cytokines, and drive pathological angiogenesis, while blocking $CD8^+$ T cell or CXCR3 restores vascular barrier function and curbs neovascularization[51]. These external observations align with our own data, central memory $CD8^+$ T cells were significantly enriched in DR samples, implicating this subset in the immune changes accompanying the disease. Conversely, we found decreased monocyte infiltration and a negative correlation between *Stat3* expression and monocyte abundance, pointing to an immunosuppressive microenvironment in line with the reported predominance of M2 macrophages in PDR.

Clinical and experimental evidence has established DR as a chronic low-grade inflammatory disease in which inflammatory mediators drive pathogenesis[52]. At its core, DR is a coordinated inflammatory disease. Leukocyte stasis and infiltration by innate and adaptive immune cells, microglial activation, mobilization of the complement and coagulation cascades, and a broad rise in cytokines and chemokines[53]. Tumor necrosis factor (TNF)-α, secreted by macrophages, NK cells, and T cells, links inflammation to neovascularization and is an established DR biomarker[54]. Yun *et al*[55] showed that activated STAT3 increased TNF-α production in microglia and thereby induce pericyte apoptosis. Tregs appear to counteract these processes: finerenone expands the Treg population, lowers pro-inflammatory mediators, and mitigates RNV and vascular leakage[56], and that expanding Tregs systemically spares the *db*/*db* mouse retina from neurodegeneration, gliosis, inflammatory changes, and barrier leakage[57]. The Treg reduction we observed is consistent with such a protective role and marks Treg restoration as a candidate intervention strategy for DR.

In tumors, RNA modifications remodel the microenvironment toward immunosuppression and angiogenesis, aggravating hypoxia, metabolic stress, and impaired drug delivery, thereby contributing to breast cancer heterogeneity and treatment resistance[58]. The *m⁶A* methylation supports adaptation to hypoxia, drives metabolic reprogramming, and reshapes immune phenotypes, together establishing an immunosuppressive microenvironment conducive to tumor proliferation and metastasis, and the *m⁶A*-targeted approaches are emerging as immunotherapy options[59]. Whether analogous mechanisms operate in the hypoxic retina remains largely unknown and still requires further research. Our correlations between RNA modification-related hub genes and specific immune cell types, together with this literature, point to such a link in DR. One plausible route runs through hypoxia-inducible factor (HIF)-1α/VEGF signaling, which is enhanced in the hypoxic, high-glucose retina, where it activates endothelial cells and favors immune cell adhesion and migration. In an analogous manner, RNA modification could shape the diabetic retinal environment by adjusting the stability and translational efficiency of mRNAs encoding hypoxia-responsive proteins, chemokines, and inflammatory mediators.

Therapeutic Implications and Drug Targets Quercetin stands out among the candidate drugs for its anti-inflammatory and antioxidant activities[60]. By acting on targets that include Jun proto-oncogene, AP-1 transcription factor subunit (JUN), mitogen-activated protein kinase 1 (MAPK1), and STAT3, it dampens receptor for advanced glycation end-products (RAGE) pathway activity, which in turn strengthens cellular

resistance to oxidative stress and lessens the severity of DR[61]. Chai *et al*[62] found that quercetin increased retinal ganglion cell number and retinal layer thickness compared with vehicle-treated controls in rats rendered diabetic by streptozotocin injection, and its anti-inflammatory, anti-angiogenic, and neuroprotective effects have been linked to heme oxygenase-1 upregulation and suppression of the high-mobility group box 1 (HMGB1)/Toll-like receptor 4 (TLR4)/nuclear factor-κB (NF-κB)/NOD-like receptor protein 3 (NLRP3) inflammasome axis. At the cellular level, Zou *et al*[63] confirmed that quercetin preconditioning suppresses microglial activation and drives M2 polarization by acting on the ERK/STAT3 pathway, relieving retinal inflammation and protecting photoreceptors and the blood-retinal barrier. Wu *et al*[61] showed that quercetin likewise attenuates H_2O_2-induced injury through its antioxidative activity in ARPE-19 cells. How quercetin might be combined with existing therapeutic agents for DR remains to be examined.

Limitations and Perspectives of the Present Study Certain limitations warrant consideration when interpreting these findings. First, the analysis relied on public databases of limited sample size, so the identified DEGs, hub genes, and their estimated diagnostic performance may be unstable or over-optimistic in the absence of independent validation. Second, hub gene expression was examined only in an *in vitro* model under high glucose, a simplified setting that cannot reproduce the cellular complexity of the retina; without functional experiments, only correlative conclusions are possible. Third, clinical samples and animal models remain to be examined, and the immune cell estimates, being computational, await direct verification. Future work will verify the candidate genes in DR animal models and clinical samples, define the functions and mechanisms of the differentially expressed A&RMRGs, and examine the roles of drugs, TFs, and microRNAs *in vivo* and *in vitro*.

This study suggests that dysregulation of RNA modification and immune homeostasis are both implicated in the pathological neovascularization of DR. An inflammatory shift in retinal immune cell composition was accompanied by upregulation of the seven hub genes (*Wdr3*, *Sdad1*, *Gnl2*, *Stat3*, *Nhp2*, *Crebbp*, and *Hsp90aa1*), which showed good diagnostic value and were connected to candidate drugs such as quercetin through the STAT3 pathway. These hub genes warrant further investigation as potential therapeutic targets.

ACKNOWLEDGEMENTS

We are grateful to Dr. Tian-Long Zhang and Dr. Hai-Long Li of Fudan University for their technical guidance with the experimental procedures.

Authors' Contributions: Wang X designed the study, wrote the original draft, interpreted the data, and discussed the results. Wu DP designed the study, analyzed the data, and performed the statistical evaluation. Li R and Chen RR reviewed the literature, contributed to the study conception, and acquired the data. Lou W and Du W contributed to the study design, data collection, and analysis. Li Q and Liao YJ drafted the manuscript and critically revised it for important intellectual content. Li XM acquired the data and performed the statistical evaluation. Zhang JL and Cui HP supervised the study, critically revised the manuscript, and gave final approval of the version to be published. Wang X and Wu DP contributed equally to this work. All authors read and approved the final manuscript. Wang X and Wu DP contributed equally to this article. Correspondence should be addressed to Cui HP and Zhang JL.

Data Availability Statement: All data analyzed in this study are openly accessible: GSE12610, GSE87433, and GSE111465 can be retrieved from the GEO database, and the supplementary files accompany the online article. Any further information required to reproduce these findings is available from the corresponding author upon reasonable request.

AI-Generated Content Disclosure: ChatGPT (OpenAI) was used solely to improve the clarity of the English text during manuscript preparation. It was not involved in designing the study, collecting or analyzing the data, preparing the figures, or generating any scientific content. The authors reviewed and edited every AI-assisted passage and take full responsibility for the integrity and accuracy of the work.

Conflicts of Interest: Wang X, None; **Wu DP,** None; **Du W,** None; **Li R,** None; **Lou W,** None; **Chen RR,** None; **Liao YJ,** None; **Li Q,** None; **Li XM,** None; **Cui HP,** None; **Zhang JL,** None.

REFERENCES

1 Tan GSW, Jonas JB, Sabanayagam C, *et al*. global prevalence of diabetic retinopathy and projection of burden through 2045: systematic review and Meta-analysis. *Ophthalmology* 2021;128(11): 1580-1591.

2 Gucciardo E, Loukovaara S, Salven P, *et al*. Lymphatic vascular structures: a new aspect in proliferative diabetic retinopathy. *Int J Mol Sci* 2018;19(12):4034.

3 Sivaprasad S, Sen S, Cunha-Vaz J. Perspectives of diabetic retinopathy-challenges and opportunities. *Eye* (*Lond*) 2023;37(11):2183-2191.

4 Raman R, Ramasamy K, Shah U. A paradigm shift in the management approaches of proliferative diabetic retinopathy: role of anti-VEGF therapy. *Clin Ophthalmol* 2022;16:3005-3017.

5 Milluzzo A, Maugeri A, Barchitta M, *et al*. Epigenetic mechanisms in type 2 diabetes retinopathy: a systematic review. *Int J Mol Sci* 2021;22(19):10502.

6 Luo X, Xue DX. Potential mechanisms of epigenetic regulation in diabetic retinopathy from the perspectives of multi-omics. *Diabetol Metab Syndr* 2025;17(1):155.

7 Tang JL, Zhou CD, Ye FX, *et al*. RNA methylation homeostasis in ocular diseases: All eyes on Me. *Prog Retin Eye Res* 2025;105:101335.

8 Zhu XY, Zhou CD, Zhao SZ, *et al*. Role of M6A methylation in retinal diseases. *Exp Eye Res* 2023;231:109489.

9 Bai YH, Jiao XH, Hu JG, *et al*. WTAP promotes macrophage recruitment and increases VEGF secretion *via* N6-methyladenosine modification in corneal neovascularization. *Biochim Biophys Acta BBA Mol Basis Dis* 2023;1869(6):166708.

10 Friedrichs P, Schlotterer A, Sticht C, *et al*. Hyperglycaemic memory affects the neurovascular unit of the retina in a diabetic mouse model. *Diabetologia* 2017;60(7):1354-1358.

11 Davis S, Meltzer PS. GEOquery: a bridge between the gene expression omnibus (GEO) and BioConductor. *Bioinformatics* 2007;23(14): 1846-1847.

12 Su ZX, He YF, You LJ, *et al*. Coupled scRNA-seq and Bulk-seq reveal the role of HMMR in hepatocellular carcinoma. *Front Immunol* 2024;15:1363834.

13 Leek JT, Johnson WE, Parker HS, *et al*. The sva package for removing batch effects and other unwanted variation in high-throughput experiments. *Bioinformatics* 2012;28(6):882-883.

14 Stelzer G, Rosen N, Plaschkes I, *et al*. The GeneCards suite: from gene data mining to disease genome sequence analyses. *Curr Protoc Bioinformatics* 2016;54:1.30.1-1.30.33.

15 Han XY, Zhao YY, Chen SF, *et al*. Neutrophil CD11b is a pivotal PANoptosis marker correlated with disease activity in antineutrophil cytoplasmic antibody-associated vasculitis. *Apoptosis* 2025;30(11-12): 3115-3128.

16 Pan JF, Huang ZD, Xu YQ. M5C RNA methylation regulators predict prognosis and regulate the immune microenvironment in lung squamous cell carcinoma. *Front Oncol* 2021;11:657466.

17 Zhao MX, Shen S, Xue C. A novel M1A-score model correlated with the immune microenvironment predicts prognosis in hepatocellular carcinoma. *Front Immunol* 2022;13:805967.

18 Yu GC, Wang LG, Han YY, *et al*. clusterProfiler: an R package for comparing biological themes among gene clusters. *OMICS* 2012;16(5):284-287.

19 Kanehisa M, Goto S. KEGG: Kyoto encyclopedia of genes and genomes. *Nucleic Acids Res* 2000;28(1):27-30.

20 Mi HY, Muruganujan A, Ebert D, *et al*. PANTHER version 14: more genomes, a new PANTHER GO-slim and improvements in enrichment analysis tools. *Nucleic Acids Res* 2019;47(D1):D419-D426.

21 Tilford CA, Siemers NO. Gene set enrichment analysis. *Methods Mol Biol* 2009;563:99-121.

22 Liberzon A, Subramanian A, Pinchback R, *et al*. Molecular signatures database (MSigDB) 3.0. *Bioinformatics* 2011;27(12):1739-1740.

23 Szklarczyk D, Gable AL, Lyon D, *et al*. STRING v11: protein–protein association networks with increased coverage, supporting functional discovery in genome-wide experimental datasets. *Nucleic Acids Res* 2019;47(D1):D607-D613.

24 Shannon P, Markiel A, Ozier O, *et al*. Cytoscape: a software environment for integrated models of biomolecular interaction networks. *Genome Res* 2003;13(11):2498-2504.

25 Chin CH, Chen SH, Wu HH, *et al*. cytoHubba: identifying hub objects and sub-networks from complex interactome. *BMC Syst Biol* 2014;8(Suppl 4):S11.

26 Yang X, Li YH, Lv RL, *et al*. Study on the multitarget mechanism and key active ingredients of herba siegesbeckiae and volatile oil against rheumatoid arthritis based on network pharmacology. *Evid Based Complement Alternat Med* 2019;2019:8957245.

27 Chen YH, Wang XW. miRDB: an online database for prediction of functional microRNA targets. *Nucleic Acids Res* 2020;48(D1):D127-D131.

28 Zhou KR, Liu S, Sun WJ, *et al*. ChIPBase v2.0: decoding transcriptional regulatory networks of non-coding RNAs and protein-coding genes from ChIP-seq data. *Nucleic Acids Res* 2017;45(D1): D43-D50.

29 Grondin CJ, Davis AP, Wiegers JA, *et al*. Predicting molecular mechanisms, pathways, and health outcomes induced by Juul e-cigarette aerosol chemicals using the Comparative Toxicogenomics Database. *Curr Res Toxicol* 2021;2:272-281.

30 Xiao B, Liu LY, Li AY, *et al*. Identification and verification of immune-related gene prognostic signature based on ssGSEA for osteosarcoma. *Front Oncol* 2020;10:607622.

31 Bindea G, Mlecnik B, Tosolini M, *et al*. Spatiotemporal dynamics of intratumoral immune cells reveal the immune landscape in human cancer. *Immunity* 2013;39(4):782-795.

32 Liu WJ, Xie A, Xiong J, *et al*. WDR3 promotes stem cell-like properties in prostate cancer by inhibiting USF_2-mediated transcription of RASSF1A. *J Gene Med* 2023;25(7):e3498.

33 Gong LH, Yu LY, Gong XH, *et al*. Exploration of anti-inflammatory mechanism of forsythiaside A and forsythiaside B in $CuSO_4$-induced inflammation in zebrafish by metabolomic and proteomic analyses. *J Neuroinflammation* 2020;17(1):173.

34 Chen W, Zhang LS, Zhong GD, *et al*. Regulation of microglia inflammation and oligodendrocyte demyelination by Engeletin *via* the TLR4/RRP9/NF-κB pathway after spinal cord injury. *Pharmacol Res* 2024;209:107448.

35 Dong YW, Cai QQ, Fu LS, *et al*. Study of the G protein nucleolar 2 value in liver hepatocellular carcinoma treatment and prognosis. *Biomed Res Int* 2021;2021:4873678.

36 Zhu Y, Wang Z, Li YN, *et al*. The role of CREBBP/EP300 and its therapeutic implications in hematological malignancies. *Cancers (Basel)* 2023;15(4):1219.

37 Tao YL, Zhu HB, Peng YR, *et al*. Single-cell transcriptomics reveals that RNA pseudouridylation-related gene NHP2 promotes the progression of uveal melanoma and validated *in vivo* and *in vitro*. *Exp Eye Res* 2025;259:110578.

38 Yang N, Zhang NZ, Lu GJ, *et al*. RNA-binding proteins potentially regulate the alternative splicing of cell cycle-associated genes in proliferative diabetic retinopathy. *Sci Rep* 2024;14(1):6731.

39 Yan Y, Yang HJ, Wei QN, *et al*. Single-cell RNA sequencing reveals the role of heat shock protein 90AA1 in Müller cell proliferation *via* the Necroptosis/MAPK pathway in diabetic retinopathy. *Exp Eye Res* 2025;258:110508.

40 Fang YH, Wang QH, Zhang LY, *et al*. SIPA1 promotes angiogenesis by regulating VEGF secretion in Müller cells through STAT3 activation. *Heliyon* 2024;10(2):e24869.

41 Zhao N, Gui X, Fang Q, *et al*. Graphene quantum dots rescue angiogenic retinopathy *via* blocking STAT3/Periostin/ERK signaling. *J Nanobiotechnology* 2022;20(1):174.

42 Xu Q, Briggs J, Park S, *et al*. Targeting Stat3 blocks both HIF-1 and VEGF expression induced by multiple oncogenic growth signaling pathways. *Oncogene* 2005;24(36):5552-5560.

43 Li X, Cai Y, Wang YS, *et al*. Hyperglycaemia exacerbates choroidal neovascularisation in mice *via* the oxidative stress-induced activation of STAT3 signalling in RPE cells. *PLoS One* 2012;7(10):e47600.

44 Vanlandingham PA, Nuno DJ, Quiambao AB, *et al*. Inhibition of Stat3 by a small molecule inhibitor slows vision loss in a rat model of diabetic retinopathy. *Invest Ophthalmol Vis Sci* 2017;58(4):2095-2105.

45 Liu BW, Cao JL, Wu BT, *et al*. METTL3 and STAT3 form a positive feedback loop to promote cell metastasis in hepatocellular carcinoma. *Cell Commun Signal* 2023;21(1):121.

46 Pan WW, Lin F, Fort PE. The innate immune system in diabetic retinopathy. *Prog Retin Eye Res* 2021;84:100940.

47 Huang J, Zhou Q. $CD8^+$T cell-related gene biomarkers in macular edema of diabetic retinopathy. *Front Endocrinol (Lausanne)* 2022;13:907396.

48 Meng ZS, Chen YZ, Wu WY, *et al*. Exploring the immune infiltration landscape and M2 macrophage-related biomarkers of proliferative diabetic retinopathy. *Front Endocrinol (Lausanne)* 2022;13:841813.

49 Li J, Yu SS, Lu X, *et al*. The phase changes of M1/M2 phenotype of microglia/macrophage following oxygen-induced retinopathy in mice. *Inflamm Res* 2021;70(2):183-192.

50 Suvas P, Liu L, Rao P, *et al*. Systemic alterations in leukocyte subsets and the protective role of NKT cells in the mouse model of diabetic retinopathy. *Exp Eye Res* 2020;200:108203.

51 Deliyanti D, Figgett WA, Gebhardt T, *et al*. $CD8^+$ T cells promote pathological angiogenesis in ocular neovascular disease. *Arterioscler Thromb Vasc Biol* 2023;43(4):522-536.

52 Gomułka K, Ruta M. The role of inflammation and therapeutic concepts in diabetic retinopathy-a short review. *Int J Mol Sci* 2023;24(2):1024.

53 Kinuthia UM, Wolf A, Langmann T. Microglia and inflammatory responses in diabetic retinopathy. *Front Immunol* 2020;11:564077.

54 Sabanayagam C, Banu R, Chee ML, *et al*. Incidence and progression of diabetic retinopathy: a systematic review. *Lancet Diabetes Endocrinol* 2019;7(2):140-149.

55 Yun JH, Lee DH, Jeong HS, *et al*. STAT3 activation in microglia increases pericyte apoptosis in diabetic retinas through TNF-α/AKT/p70S6 kinase signaling. *Biochem Biophys Res Commun* 2022;613:133-139.

56 Jerome JR, Deliyanti D, Suphapimol V, *et al*. Finerenone, a non-steroidal mineralocorticoid receptor antagonist, reduces vascular injury and increases regulatory T-cells: studies in rodents with diabetic and neovascular retinopathy. *Int J Mol Sci* 2023;24(3):2334.

57 Llorián-Salvador M, Pérez-Martínez D, Tang M, *et al*. Regulatory T cell expansion prevents retinal degeneration in type 2 diabetes. *J Neuroinflammation* 2024;21(1):328.

58 Trnkova L, Buocikova V, Mego M, *et al*. Epigenetic deregulation in breast cancer microenvironment: Implications for tumor progression and therapeutic strategies. *Biomed Pharmacother* 2024;174:116559.

59 Zhang FS, Liu HY, Duan MQ, *et al*. Crosstalk among m^6A RNA methylation, hypoxia and metabolic reprogramming in TME: from immunosuppressive microenvironment to clinical application. *J Hematol Oncol* 2022;15(1):84.

60 Shen P, Lin WJ, Deng X, *et al*. Potential implications of quercetin in autoimmune diseases. *Front Immunol* 2021;12:689044.

61 Wu XY, Mu L, Dong ZG, *et al*. Hu-Zhang Qing-Mai Formulation anti-oxidative stress alleviates diabetic retinopathy: Network pharmacology analysis and *in vitro* experiment. *Medicine (Baltimore)* 2023;102(36):e35034.

62 Chai GR, Liu S, Yang HW, *et al*. Quercetin protects against diabetic retinopathy in rats by inducing heme oxygenase-1 expression. *Neural Regen Res* 2021;16(7):1344-1350.

63 Zou Y, Jiang JL, Li YQ, *et al*. Quercetin regulates microglia M1/M2 polarization and alleviates retinal inflammation *via* ERK/STAT3 pathway. *Inflammation* 2024;47(5):1616-1633.